Research Article | Vol. 29, No. 4 / 15 February 2021 / Optics Express 5755
Optics EXPRESS

Nonlinear dynamics in intra-cavity pumped thin-disk lasers

SARAH TRINSCHEK,[1,3,*] CHRISTIAN VORHOLT,[2,3] AND ULRICH WITTROCK[2]

[1]*Department of Engineering Physics, Münster University of Applied Sciences, Stegerwaldstraße 39, 48565 Steinfurt, Germany*
[2]*Photonics Laboratory, Münster University of Applied Sciences, Stegerwaldstraße 39, 48565 Steinfurt, Germany*
[3]*These authors contributed equally.*
[*]*s.trinschek@fh-muenster.de*

Abstract: Cross-saturation of the gain media in intra-cavity pumped lasers leads to complex dynamics of the laser power. We present experimental results and a detailed theoretical analysis of this nonlinear dynamics for an intra-cavity pumped Yb:YAG thin-disk laser in the framework of a rate-equation model. The gain medium of this laser is residing in the resonator of a conventional, diode-pumped Yb:YAG thin-disk laser. Continuous-wave operation, periodic pulse trains, and chaotic fluctuations of the optical power of both lasers were observed. The dynamics is not driven by external perturbations but arises naturally in this laser system. Further examination revealed that these modes of operation can be controlled by the resonator length of the diode-pumped laser but that the system can also show hysteresis and multi-stability.

1. Introduction

A large class of lasers shows relaxation oscillations of their output power when the laser is subjected to a rapid change of gain or loss. These lasers are often called class-B lasers [1]. Their dynamics has to be described in a two-dimensional phase space that is spanned by the population inversion in the gain medium and the laser power. An additional degree of freedom to such a laser can be added by placing a saturable absorber into the resonator. Then, passive Q-switching and even chaotic fluctuations of the power occur under suitable conditions [2]. If the saturable absorber is itself a laser gain medium and resides in its own resonator, we have an intra-cavity pumped laser. Such a system has four dynamical variables (two population inversions and two laser powers). In the past, intra-cavity pumped lasers have shown hysteresis and self-sustained oscillations of their output power [3–6]. Here, we present a detailed theoretical study and supporting experimental results of an intra-cavity pumped laser that shows continuous-wave operation, periodic oscillation of the output power, periodic pulse trains, and chaotic power fluctuations. To the best of our knowledge, this is the first study of its kind and it is meant to further the understanding and utilization of the rich dynamics of intra-cavity pumped lasers.

Intra-cavity pumping of lasers is sometimes used for pumping gain media with very low single-pass absorption of the pump light. The number of passes of the pump light through the gain medium is then only limited by the losses of the resonator mirrors of the pump laser. For a study of a laser with very low quantum defect, we pumped an Yb:YAG thin-disk laser operating at 1048 nm by another Yb:YAG thin-disk laser operating at 1030 nm. We chose intra-cavity pumping because the single-pass pump light absorption at 1030 nm was only of the order of 1% for our Yb:YAG disk [7].

Figure 1 shows the energy level diagram of Yb:YAG in (a) and the effective cross sections for absorption and emission in (b). The two electronic states $^2F_{7/2}$ and $^2F_{5/2}$ are split by the crystal field into 4 and 3 sublevels, respectively. The relative population densities at room temperature

#417154 https://doi.org/10.1364/OE.417154
Journal © 2021 Received 9 Dec 2020; revised 28 Jan 2021; accepted 28 Jan 2021; published 8 Feb 2021

Optics EXPRESS

of the sublevels of each electronic state are denoted $f_{Z1} \cdots f_{Z4}$ and $f_{A1} \cdots f_{A3}$. The intra-cavity pumped laser is pumped on the $Z_3 \rightarrow A_1$ transition (1030 nm) and emits on the $A_1 \rightarrow Z_4$ transition (1048 nm). The quantum defect is thus 2%. Strong coupling of the two Yb:YAG lasers occurs if both the pump transition and the laser transition of the Yb:YAG disk are saturated.

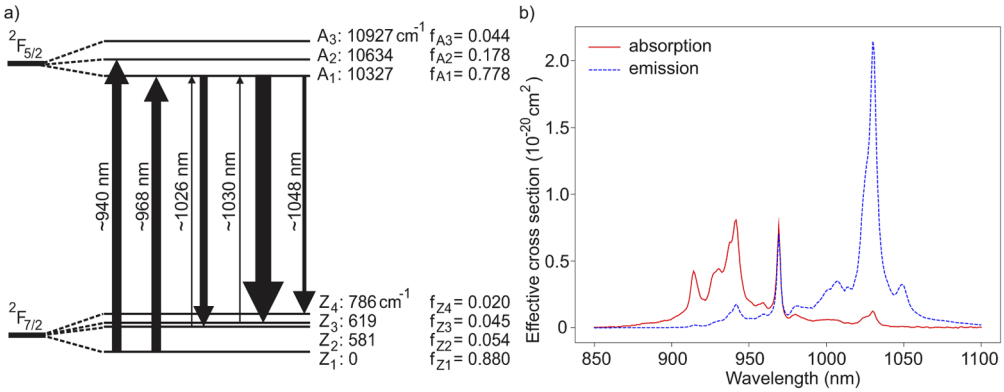

Fig. 1. (a) Energy levels of Yb:YAG at room temperature [7,8]. The energy levels are denoted by Z in the lower multiplet and by A in the upper multiplet. The relative occupation numbers are denoted by f. The thicknesses of the arrows are proportional to the effective cross sections of the transitions. (b) Effective cross sections for absorption and emission at room temperature [9].

Our intra-cavity pumped Yb:YAG laser showed surprisingly complex dynamics of the output power [10]. Among the 18 papers on intra-cavity pumped lasers we could find [3–6,11–24], only the following five discuss dynamics of the output power. Bollig *et al.* studied a Ho:YAG laser intra-cavity pumped by a Tm:YAG laser. They observed hysteresis of the laser thresholds of both lasers which they attributed to the Ho:YAG crystal acting as a saturable absorber for the Tm:YAG laser [3]. Schellhorn *et al.* were the first to report a pulse mode behaviour of both the Ho:YAG laser and the Tm:YLF laser that was pumping it intra-cavity [4]. The temporal spacing and the energy of the pulses were irregular. Yang *et al.* noticed the same behaviour in their Ho:LuAG laser [5]. In retrospect, these observations might have been signatures for chaos but that was not investigated by the authors. Chen *et al.* looked for chaotic emission in their intra-cavity pumped Tm:YAG laser but only observed unstable spiking that they attributed to the operation of their laser close to threshold [6]. However, when they replaced their Tm:YAG disk by another Yb:YAG disk, creating an Yb:YAG disk laser pumped intra-cavity to another Yb:YAG disk laser, they observed the same chaotic laser emission that we had published previously. Herault *et al.* explicitly stated that unlike Schellhorn *et al.* they did not observe any self-pulsing of their 1064 nm Nd:YVO_4 laser that was pumped intra-cavity to a 912 nm Nd:$GdVO_4$ laser [18]. None of these papers presented a theoretical analysis of the observed laser dynamics. Here, we show experimentally that the dynamics of our laser can be controlled by simply changing the resonator length of the pump laser. We provide insight into the different modes of operation of intra-cavity pumped lasers by analysing the coupled rate equations using the concepts of nonlinear dynamics.

2. Experiments

2.1. Experimental setup of the intra-cavity pumped thin-disk laser

Our experimental setup is shown in Fig. 2. The diode-pumped Yb:YAG thin-disk laser is pumped at 940 nm with 280 W of optical pumping power. A multi-pass pumping scheme establishes 16 single passes through disk 1. The resulting pump spot is circular and has a diameter of 5.5 mm.

Optics EXPRESS

The diode-pumped laser has a V-shaped resonator formed by disk 1 at the vertex of the "V", disk 2 and a dichroic mirror terminating the resonator. The opening angle of the V-shaped resonator is 10°. Consequently, the angle of incidence of the laser beam on disk 1 is 5°.

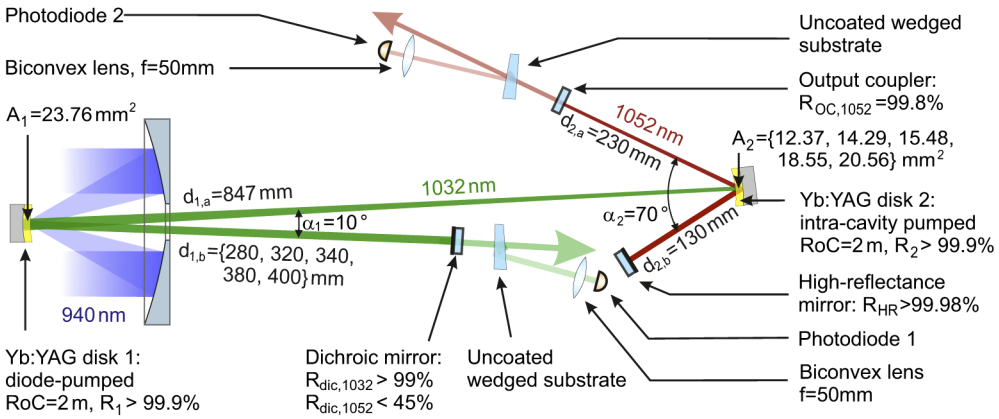

Fig. 2. Experimental setup of the two coupled lasers. The arm lengths of the V-shaped resonator of the diode-pumped laser are denoted by $d_{1,a}$ and $d_{1,b}$. The arm length of the lower arm $d_{1,b}$ is varied in the experiment. The arm lengths of the V-shaped resonator of the intra-cavity pumped laser are kept constant and are denoted by $d_{2,a}$ and $d_{2,b}$. The angle that is introduced by the double reflection inside the wedged substrates is shown exaggerated for the purpose of illustration.

The dichroic mirror is plane and has a reflectance of less than 45% at 1052 nm and a reflectance larger than 99% at 1032 nm. If the dichroic mirror was replaced by a conventional broadband high reflectance mirror, the laser would oscillate at longer wavelengths in order to reduce its absorption loss in disk 2. The intra-cavity pumped laser has its own V-shaped resonator formed by a plane high reflectance mirror, disk 2 and a plane output coupler with a transmittance of 0.2% at 1052 nm. The angle of incidence of the laser beam on disk 2 is 35 ° due to mechanical restrictions. As a consequence, the intensity distribution on disk 2 is slightly elliptical, having a circularity of 0.82.

Both disks in our experimental setup are made from Yb:YAG and are glued onto diamond heat sinks. The disks have the same thickness of 130 μm, a diameter of 14 mm, a doping concentration of 9 at.% and a concave curvature with a radius of 2 m which makes the resonators stable. A fraction of the 1032 nm laser light that is transmitted by the dichroic mirror is directed towards an uncoated wedged substrate. The second reflection of the laser light inside the wedged substrate is received by a photodiode (photodiode 1), likewise a fraction of the 1052 nm laser light transmitted by the output coupler is directed towards another uncoated wedged substrate and photodiode (photodiode 2). Both photodiodes have a bandwidth of 30 MHz.

The spectral emission of the lasers in continuous-wave operation is measured once with an optical spectrum analyzer (HP 1450B) which is used temporary in lieu of the photodiodes. Centroid wavelengths around 1032 nm and 1052 nm were measured. We have shown in a previous publication that the emission spectrum changes as the laser is pumped higher above threshold and its centroid shifts by a few nanometers [7]. Furthermore, the angle of incidence of the beams on the intra-cavity pumped disk can alter the centroid of the emission spectrum due to spatial hole burning [25]. This is true for both the 1032 nm laser and the 1052 nm laser. In [26] two of us showed that spatial hole burning also causes the spectrum of the laser emission of the Yb:YAG thin-disk lasers to be a few nanometers wide. In our rate equation model, we neglect spatial hole burning and assume monochromatic laser emission.

Optics EXPRESS

We will see that the ratio $\kappa := A_1/A_2$ of the beam areas in the disks (cf. Fig. 2) determines the dynamics of the two coupled lasers [10]. The ratio κ can be changed in our experiment by shifting the dichroic mirror along the optical axis of the resonator, i.e. we change the distance $d_{1,\mathrm{b}}$. Shifting the dichroic mirror along the optical axis also affects the ratio of the resonator round-trip times which is denoted by χ. The diameter of the fundamental mode at disk 1 is seven to ten times smaller than the pump spot for all five different arm lengths $d_{1,\mathrm{b}}$ we investigated. Since there are no apertures in the resonators, the diameter of the 1032 nm beam adapts to the pumped area. The laser operates in transverse multimode and has a constant beam area A_1 at disk 1. However, the area A_2 of this beam in disk 2 does change when $d_{1,\mathrm{b}}$ is altered. Nevertheless, the diameter of the pumped area A_2 was always four to five times larger than the fundamental mode of the intra-cavity pumped laser, thus also supporting multi-mode operation. The beam areas were calculated under the assumption that the thermal lens effect can be neglected. This assumption is well justified for both disks, because the relative change in refractive power of disk 1 is smaller than 3% in comparison to the refractive power of the cold disk for the applied pump power of 280 W [27]. The change in refractive power in disk 2 is even lower, since it exhibits a lower quantum defect and therefore lower heating.

2.2. Experimental results

The dichroic mirror was set to five different positions, $d_{1,b} = 280, 320, 340, 380$ and 400 mm resulting in five different beam areas in disk 2 and five different resonator round trip times. At each position, the dichroic mirror was aligned such that the recorded signal of photodiode 2 was maximal. The signals of photodiode 1 and photodiode 2 which are proportional to the intra-cavity laser powers of both lasers are shown in Fig. 3. At the first position of the dichroic mirror, the beam area ratio was $\kappa = 1.2$ and both lasers were running in continuous-wave mode as shown in Fig. 3(a). At the second position (see Fig. 3(b)), a beam area ratio of 1.3 was achieved. Both lasers showed self-sustained oscillations. In the following, we characterize the emission of the lasers as dP-iP cycles by counting the number of pulses after which the temporal shape of the output power curve repeats for the power of the diode-pumped laser (d) and the power of the intra-cavity pumped laser (i). The beam area ratio $\kappa = 1.3$ thus results in a 1P-1P cycle because the power of the diode-pumped laser exhibits one maximum and the power of the intra-cavity pumped laser also exhibits one maximum before the curve in Fig. 3(b) repeats. The pulsations of the two lasers are approximately in anti-phase. The diode-pumped laser is driving the population density in the intra-cavity pumped disk and the energy in the system is shifting periodically between the population densities and the light fields. The graph in Fig. 3(c) shows self-sustained pulsation with pronounced intensity peaks at a beam area ratio of 1.5. For this ratio, a 2P-2P cycle was observed in the powers of the lasers. The two-period cycle of the intra-cavity pumped laser becomes a one-period cycle for a beam area ratio of 1.7 (see Fig. 3(d)), thus we have a 2P-1P cycle. At last, a beam area ratio of 1.9 was established and chaotic laser emission was observed as shown in Fig. 3(e).

When we started the investigation of the nonlinear dynamics, we used the same experimental setup as in Vorholt et al. [7]. In this setup, the output coupler had a reflectivity of about 99.98% in order to achieve a high intra-cavity power. The output power was 10.3 W at 300 W diode pump power and the optical efficiency, which is the output power of the second laser divided by the diode pump power, was 3.4%. However, when we investigated the influence of the ratio of the beam areas, disk 2 was damaged by high intensity laser pulses. Figure 4 shows these high intensity laser pulses that are transmitted by the dichroic mirror for $\kappa = 3.1$. Consequently, we replaced the high reflectance output coupler in the second laser with a mirror having a reflectivity of 99.8% at 1052 nm to prevent damage to the replacement disk (cf. Fig. 2). This also reduces the optical efficiency to be about 3%.

Optics EXPRESS

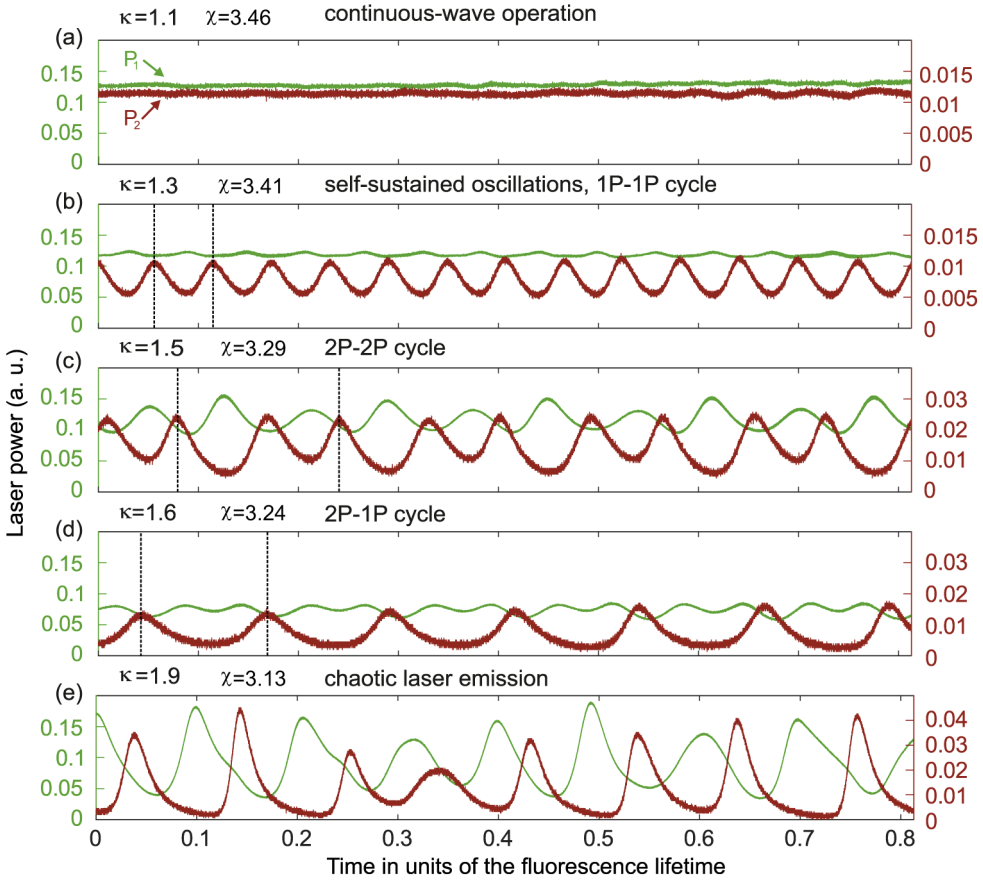

Fig. 3. Measured dynamics of the laser powers of the diode-pumped laser P_1 (green) and the intra-cavity pumped laser P_2 (red) for five different positions of the dichroic mirror, resulting in five different beam area ratios $\kappa = A_1/A_2$ and five different resonator round-trip time ratios χ. The periods of the laser power oscillations for $\kappa = 1.3$, $\kappa = 1.5$ and $\kappa = 1.7$ are indicated by vertical dashed lines. For $\kappa = 1.9$ in (e), we observe chaotic emission.

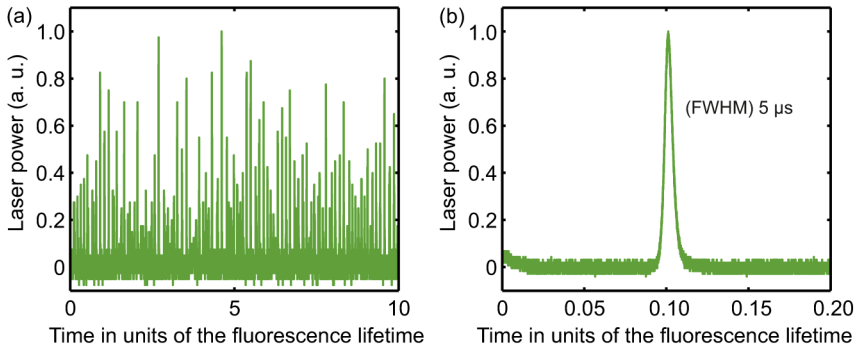

Fig. 4. Laser power transmitted by the dichroic mirror at a diode pump power of 174 W. In comparison to the experimental setup shown in Fig. 2 the output coupler with a transmittance of 0.2% had been replaced by a high reflectance mirror. The beam area ratio is $\kappa = 3.1$.

Optics EXPRESS

Qualitatively, the physical origin of the pulsing behaviour of the lasers can be explained as follows. A spike in the power of the diode-pumped laser can lead to gain-switching of the intra-cavity pumped laser. Also, disk 2 serves as a saturable absorber for the diode-pumped laser and can force it into periodic Q-switching. The intensity of the diode-pumped laser that is required to bleach this absorber depends on the population of the Z_3 sublevel of disk 2 (cf. Fig. 1). This population in turn depends on the laser intensity of the intra-cavity pumped laser which re-populates the ${}^2F_{7/2}$-manifold by stimulated emission. Thus, both laser intensities act on each other.

3. Rate-equation model

3.1. Dimensional model equations

In the following, we present a model for the intra-cavity pumped Yb:YAG thin-disk laser. The continuous-wave output power of intra-cavity lasers with high round trip gain was studied by Brown [28,29] using a Rigrod approach. Here, we develop a model that is capable to capture the temporal dynamics of the system. It consists of four coupled rate equations for the time evolution of the population densities of the excited state in the first, diode-pumped disk n_1 and in the second, intra-cavity pumped disk n_2 as well as the laser intensities in the disks of the diode-pumped laser I_1 and the intra-cavity pumped laser I_2. It uses the small gain approximation for thin or diluted media. Figure 5 schematically shows the main constituents of the model. In the following, quantities characterizing the first, diode-pumped laser are indicated by the subscript 1 and quantities characterizing the second, intra-cavity pumped laser are indicated by the subscript 2.

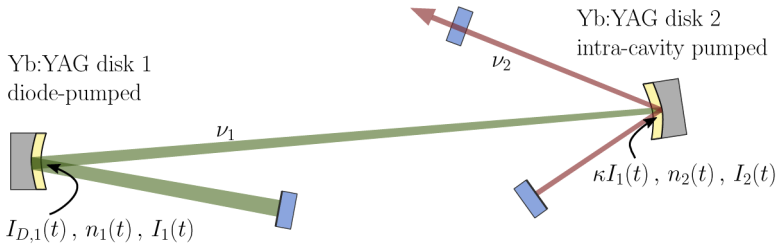

Fig. 5. Schematic representation of the main constituents of the rate-equation model. The population densities in the upper manifold of the first, diode-pumped and the second, intra-cavity pumped disk are denoted by n_1 and n_2, respectively. The laser light in the disks has the intensity I_1 (shown in green) and I_2 (shown in red) and the frequency ν_1 and ν_2, respectively. The laser diodes have been omitted from the drawing for clarity since they just provide an effective pump intensity $I_{D,1}(t)$ in disk 1.

In the derivation of the model, we assume monochromatic laser light with flat-top intensity distributions for both lasers. We use effective cross sections in order to account for the distribution of the atoms across the sublevels of each manifold. Amplified spontaneous emission (ASE) can compete with the laser oscillation in a strongly pumped Yb:YAG thin-disk laser if resonator losses are high. In this case, the laser power circulating in the resonator becomes so weak that its gain competition with ASE trapped by total internal reflection in the disk has to be considered. In our experiment, the diode-pumped laser had approximately 2% round-trip losses from absorption in the second disk plus 1% loss at its dichroic mirror. The intra-cavity pumped laser only had 0.4% combined losses per round trip at the output coupler and the coating of the laser disk. These losses are lower than the resonator losses of the conventional diode-pumped thin-disk lasers from which our disks were taken and which showed no signs of ASE. We therefore do not need to consider ASE in our model. Both disks in our experimental setup have identical

Optics EXPRESS

doping concentrations n_{dot} and we assume that they are operated at approximately the same temperatures. This assumption is supported by measurements with a calibrated IR-camera, which yield a temperature difference of less than 10 K. Then, the fluorescence lifetimes are identical for both disks and denoted by τ_{10} in the following. Under these conditions, also the effective cross sections for absorption and stimulated emission have the same values in both disks at a given wavelength. Therefore, $\sigma_{\mathrm{a},\nu}$ is the effective cross section for absorption of light of frequency ν in both disks and $\sigma_{\mathrm{e},\nu}$ is the corresponding effective cross section for stimulated emission.

The population density of the excited state in the first disk, n_1, results from absorption and stimulated emission at the wavelengths of diode light and laser light, as well as from spontaneous emission. Its time derivative is thus given by

$$\frac{\mathrm{d}n_1}{\mathrm{d}t} = \underbrace{\frac{I_{\mathrm{D},1}}{h\nu_{\mathrm{D}}}\left[\sigma_{\mathrm{a},\nu_{\mathrm{D}}}\left(n_{\mathrm{dot}}-n_1\right)-\sigma_{\mathrm{e},\nu_{\mathrm{D}}}\,n_1\right]}_{\text{absorption and stim. emission at } \nu_{\mathrm{D}}} + \underbrace{\frac{M_{1,1}I_1}{h\nu_1}\left[\sigma_{\mathrm{a},\nu_1}\left(n_{\mathrm{dot}}-n_1\right)-\sigma_{\mathrm{e},\nu_1}\,n_1\right]}_{\text{stim. emission and reabsorption at } \nu_1} \underbrace{-\frac{n_1}{\tau_{10}}}_{\text{spont. em.}}, \quad (1)$$

where h is the Planck constant, ν_{D} and ν_1 are the optical frequencies of the diode light and the light of the first laser respectively, and $M_{1,1}$ is the number of passes of the laser light through disk 1 per round trip. The laser intensities $I_{\mathrm{D},1}$ and I_1 (and later I_2) are assumed to have no spatial variation in the disks. The effective pump light intensity $I_{\mathrm{D},1}$ impinging onto disk 1 is the result of all overlapping beams of the diode multi-pass pumping scheme. It is related to the pump intensity $I_{D,0}$ that would hit disk 1 if single-pass pumping were used via [30]

$$I_{\mathrm{D},1}\left[\sigma_{\mathrm{a},\nu_{\mathrm{D}}}\left(n_{\mathrm{dot}}-n_1\right)-\sigma_{\mathrm{e},\nu_{\mathrm{D}}}\,n_1\right]d = I_{D,0}\left(1-\exp\left\{-M_{\mathrm{D},1}d[\sigma_{\mathrm{a},\nu_{\mathrm{D}}}\left(n_{\mathrm{dot}}-n_1\right)-\sigma_{\mathrm{e},\nu_{\mathrm{D}}}\,n_1]\right\}\right), \quad (2)$$

where $M_{\mathrm{D},1}$ is the number of passes of the diode light through disk 1 which is 16 in our case. The intensities I_1 and I_2 of the laser light in the resonators are in the small gain approximation given by the sum of the intensities of forwards and backwards propagating laser beams in the respective resonators. The time evolution of I_1 is determined by

$$\begin{aligned}\frac{\mathrm{d}I_1}{\mathrm{d}t} = \frac{I_1}{T_1}\Bigg\{&\underbrace{M_{1,1}d\left[\sigma_{\mathrm{e},\nu_1}\,n_1-\sigma_{\mathrm{a},\nu_1}\left(n_{\mathrm{dot}}-n_1\right)\right]}_{\substack{\text{stim. emission and reabsorption}\\ \text{in disk 1}}}\\ &\underbrace{-M_{1,2}d\frac{A_1}{A_2}\left[\sigma_{\mathrm{a},\nu_1}\left(n_{\mathrm{dot}}-n_2\right)-\sigma_{\mathrm{e},\nu_1}\,n_2\right]}_{\substack{\text{absorption and stim. emission}\\ \text{in disk 2}}}\underbrace{-\gamma_{\mathrm{diss},1}}_{\text{diss. loss}}\Bigg\}+\underbrace{k_{\mathrm{sp},1}\frac{n_1}{\tau_{10}}}_{\text{spont. em.}},\end{aligned} \quad (3)$$

where T_1 is the resonator round-trip time of the first laser and $M_{1,2}$ is the number of passes of the light from the first laser through disk 2 per round trip. When expanded, Eq. (3) contains the product $I_1 \cdot A_1/A_2$ which is the intensity of the first laser beam on disk 2. The beam area ratio $\kappa = A_1/A_2$ thereby determines the coupling strength between the population density n_2 in disk 2 and the intensity I_1 of the laser light in disk 1. The dissipative loss $\gamma_{\mathrm{diss},1} = -\ln[R_{\mathrm{dic}}R_1^{(M_{1,1}/2)}R_2^{(M_{1,2}/2)}(1-L_1)^2]$ is determined by the reflectivity R_{dic} of the dichroic mirror, R_1 of the high-reflection coating on the backside of disk 1, R_2 of the high-reflection coating on the backside of disk 2, and the losses L_1 due to scattering and imperfections in the disks. Spontaneous emission into the laser mode is accounted for by multiplying the rate of spontaneous emission by the factor $k_{\mathrm{sp},1}$ which contains the fractional solid angle.

The population density of the excited state in disk 2 follows the rate equation

$$\frac{\mathrm{d}n_2}{\mathrm{d}t} = \kappa\underbrace{\frac{M_{1,2}I_1}{h\nu_1}\left[\sigma_{\mathrm{a},\nu_1}(n_{\mathrm{dot}}-n_2)-\sigma_{\mathrm{e},\nu_1}n_2\right]}_{\text{absorption and stim. emission at } \nu_1} + \underbrace{\frac{M_{2,2}I_2}{h\nu_2}\left[\sigma_{\mathrm{a},\nu_2}(n_{\mathrm{dot}}-n_2)-\sigma_{\mathrm{e},\nu_2}n_2\right]}_{\text{absorption and stim. emission at } \nu_2} \underbrace{-\frac{n_2}{\tau_{10}}}_{\text{spont. em.}}, \quad (4)$$

Optics EXPRESS

where ν_2 is the optical frequency of the light of the second laser and $M_{2,2}$ is the number of passes of laser light of the second laser through disk 2 per round trip. The model is completed by the rate equation for the laser intensity I_2 in disk 2

$$\frac{\mathrm{d}I_2}{\mathrm{d}t} = \underbrace{\frac{I_2}{T_2}\Big\{M_{2,2}d\left[\sigma_{\mathrm{e},\nu_2}n_2 - \sigma_{\mathrm{a},\nu_2}(n_{\mathrm{dot}} - n_2)\right]}_{\text{stim. emission and reabs. in disk 2}} \underbrace{-\gamma_{\mathrm{diss},2}}_{\text{diss. losses}} \underbrace{-\gamma_{\mathrm{out},2}\Big\}}_{\text{outcoupling}} + \underbrace{k_{\mathrm{sp},2}\frac{n_2}{\tau_{10}}}_{\text{spont. em.}}, \tag{5}$$

where T_2 is the resonator round-trip time of the second laser. The losses are composed of an outcoupling term $\gamma_{\mathrm{out},2} = -\ln(R_{\mathrm{OC}})$ determined by the reflectivity R_{OC} of the outcoupling mirror and the dissipative loss $\gamma_{\mathrm{diss},2} = -\ln[R_{\mathrm{HR}}R_2^{(M_{2,2}/2)}(1-L_2)^2]$ where R_{HR} is the reflectivity of the high-reflectance mirror (cf. Fig. 2). L_2 is the parasitic loss due to scattering and absorption.

For the calculation of $\gamma_{\mathrm{diss},1}$ and $\gamma_{\mathrm{diss},2}$ we assume a reflectivity of 100% for the coatings on the backside of both disks as well as for the HR resonator mirror of the second laser. The parasitic losses $L_1 = 5.4 \cdot 10^{-3}$ and $L_2 = 95 \cdot 10^{-6}$ have been determined by comparing the output power of numerical simulations as a function of L_1 and L_2 to the measured output power of the laser presented in Vorholt et al. [7]. The large difference in parasitic loss may be caused by the fact that disk 1 was more than six years old and disk 2 had been refurbished just before the experiments were carried out.

All parameters of the model and their values in the simulations are summarized in Table 1.

3.2. Dimensionless equations

In order to analyze the model, the equations are written in a dimensionless form by applying a scaling. We introduce normalized population densities that reach unity when the disks are transparent at the laser wavelength of the first laser and second laser. The intensities are normalized by their respective saturation intensities [32]

$$I_{\mathrm{sat},1} = \frac{h\nu_1}{\tau_{10}}\frac{1}{\sigma_{\mathrm{a},\nu_1} + \sigma_{\mathrm{e},\nu_1}} \quad \text{and} \quad I_{\mathrm{sat},2} = \frac{h\nu_2}{\tau_{10}}\frac{1}{\sigma_{\mathrm{a},\nu_2} + \sigma_{\mathrm{e},\nu_2}}. \tag{6}$$

We apply the scaling

$$\tau = \frac{t}{\tau_{10}} \qquad D_1 = \frac{n_1}{n_{\mathrm{dot}}\beta_{\nu_1}} \qquad D_2 = \frac{n_2}{n_{\mathrm{dot}}\beta_{\nu_2}} \qquad i_1 = \frac{I_1}{I_{\mathrm{sat},1}} \qquad i_2 = \frac{I_2}{I_{\mathrm{sat},2}}, \tag{7}$$

where the cross-section ratios

$$\beta_{\nu_1} = \frac{\sigma_{\mathrm{a},\nu_1}}{\sigma_{\mathrm{a},\nu_1} + \sigma_{\mathrm{e},\nu_1}} \quad \text{and} \quad \beta_{\nu_2} = \frac{\sigma_{\mathrm{a},\nu_2}}{\sigma_{\mathrm{a},\nu_2} + \sigma_{\mathrm{e},\nu_2}} \tag{8}$$

physically correspond to the fractions of ions of the second laser necessary in the upper state to be transparent at the pump and lasing wavelength. In this scaling, the rate equations for the dimensionless quantities read

$$\frac{\mathrm{d}D_1}{\mathrm{d}\tau} = \frac{i_{\mathrm{D},0}B_1M_{\mathrm{D},1}}{W^{(p)}}\left\{1 - \exp\left[-W_{\mathrm{D},1}\left(1 - \frac{D_1}{B_1}\right)\right]\right\} - M_{1,1}i_1(D_1 - 1) - D_1 \tag{9}$$

$$\frac{\mathrm{d}i_1}{\mathrm{d}\tau} = \frac{i_1}{\Gamma_1}\left[W_1\left(D_1 - 1\right) - \kappa\frac{M_{1,2}}{M_{1,1}}W_1\left(1 - \frac{D_2}{B_2}\right) - \gamma_{\mathrm{diss},1}\right] + \eta_1 D_1 \tag{10}$$

$$\frac{\mathrm{d}D_2}{\mathrm{d}\tau} = M_{1,2}\,\kappa\,i_1\left(B_2 - D_2\right) - M_{2,2}i_2\left(D_2 - 1\right) - D_2 \tag{11}$$

$$\frac{\mathrm{d}i_2}{\mathrm{d}\tau} = \frac{i_2\chi}{\Gamma_1}\left[W_2(D_2 - 1) - \gamma_{\mathrm{diss},2} - \gamma_{\mathrm{out},2}\right] + \eta_2 D_2\,, \tag{12}$$

where we used Eq. (2) and introduced the following dimensionless parameters as defined in Table 1: The diode pump intensity normalized by the saturation intensity of the diode-pumped

Optics EXPRESS

Table 1. Definition of the parameters of the rate-equation model and their values used in the numerical simulations. $c_0 = 3 \cdot 10^8$m/s is the speed of light in vacuum.

Symbol	Description	Value
ν_D	optical frequency of the diode laser	c_0 / 940 nm
ν_1	optical frequency of the first laser	c_0 / 1032 nm
ν_2	optical frequency of the second laser	c_0 / 1051 nm
σ_a, ν_D	effective cross section for absorption at 940 nm [9]	$6.97 \cdot 10^{-21}$ cm^2
σ_e, ν_D	effective cross section for stimulated emission at 940 nm [9]	$1.45 \cdot 10^{-21}$ cm^2
σ_{a,ν_1}	effective cross section for absorption at 1032 nm [9]	$0.686 \cdot 10^{-21}$ cm^2
σ_{e,ν_1}	effective cross section for stimulated emission at 1032 nm [9]	$13.0 \cdot 10^{-21}$ cm^2
σ_{a,ν_2}	effective cross section for absorption at 1051 nm [9]	$68.5 \cdot 10^{-24}$ cm^2
σ_{e,ν_2}	effective cross section for stimulated emission at 1051 nm [9]	$2.96 \cdot 10^{-21}$ cm^2
τ_{10}	fluorescence lifetime at 300 K [31]	958 μs
$M_{1,1}$	number of passes of the laser light through disk 1 per round trip	4
$M_{2,2}$	number of passes of the laser light through disk 2 per round trip	4
$M_{1,2}$	number of passes of the pump light through disk 2 per round trip	2
$M_{D,1}$	number of passes of the pump light through disk 1	16
d	thickness of disk 1 and disk 2	130 μm
$\gamma_{diss,1}$	dissipative loss of the first laser	$19.6 \cdot 10^{-3}$
$\gamma_{diss,2}$	dissipative loss of the second laser	$0.202 \cdot 10^{-3}$
$\gamma_{out,2}$	outcoupling loss of the second laser	$2.00 \cdot 10^{-3}$
T_1	round-trip time in the resonator of the first laser	3.33 ns
$\chi = T_1/T_2$	ratio of the resonator round-trip times	0..25
$\kappa = A_1/A_2$	ratio of the beam areas on the disks	1..3
$i_{D,0} = I_{D,0} \frac{\tau_{10}(\sigma_{a,\nu_D}+\sigma_{e,\nu_D})}{h\nu_D}$	pumping intensity of the diode laser normalized by the saturation intensity of the first laser	0.0482
$B_1 = \frac{\sigma_{a,\nu_D}}{\sigma_{a,\nu_1}} \frac{\sigma_{a,\nu_1}+\sigma_{e,\nu_1}}{\sigma_{a,\nu_D}+\sigma_{e,\nu_D}}$	quotient of the cross-section ratios of disk 1	16.5
$B_2 = \frac{\sigma_{a,\nu_1}}{\sigma_{a,\nu_2}} \frac{\sigma_{a,\nu_2}+\sigma_{e,\nu_2}}{\sigma_{a,\nu_1}+\sigma_{e,\nu_1}}$	quotient of the cross-section ratios of disk 2	2.22
$W_{D,1} = M_{D,1} d \sigma_{a,\nu_D} n_{dot}$	measure for the absorbed fraction of pump light in disk 1 (given by $\left[1 - \exp(-W_{D,1})\right]$)	1.81
$W_1 = M_{1,1} d \sigma_{a,\nu_1} n_{dot}$	reabsorption of 1032 nm light in disk 1	$44.6 \cdot 10^{-3}$
$W_2 = M_{2,2} d \sigma_{a,\nu_2} n_{dot}$	reabsorption of 1051 nm light in disk 2	$4.44 \cdot 10^{-3}$
$\eta_1 = \frac{n_{dot}\beta_{\nu_1}}{I_{sat,1}} k_{sp,1}$	rate of spontaneous emission at 1032 nm in the first laser	$200 \cdot 10^{-12}$
$\eta_2 = \frac{n_{dot}\beta_{\nu_2}}{I_{sat,2}} k_{sp,2}$	rate of spontaneous emission at 1051 nm in the second laser	$200 \cdot 10^{-12}$
$\Gamma_1 = T_1/\tau_{10}$	resonator round-trip time of the first laser normalized by the lifetime of the excited state	$3.48 \cdot 10^{-6}$

transition is denoted $i_{D,0}$. The parameters $W_{D,1}$, W_1 and W_2 are measures for the absorption of the disks at the wavelength of the diode laser, the first laser and the second laser, respectively. The parameters B_1 and B_2 are the ratios of the transparency thresholds for the pump light and for the emitted laser light in disk 1 and disk 2, respectively. The effective cross sections for absorpion and stimulated emission entering these parameters are obtained from a smoothed interpolation of the data in [9]. Γ_1 is the resonator round-trip time normalized by the fluorescence lifetime. We define $\chi = T_1/T_2$ as the ratio of the round-trip times. This ratio affects the coupling strength between the population density n_2 and the intensity I_2 in disk 2. For a longer resonator round-trip time T_2, and thus smaller value of χ, the laser light spends a smaller fraction of the round-trip

Optics EXPRESS

time in disk 2, where the stimulated emission and reabsorption processes take place that couple I_2 to n_2. Throughout the analysis of the model, we fix all parameters to the values given in Table 1 and only vary the normalized pump intensity $i_{\mathrm{D},0}$, the ratio of the resonator round-trip times $\chi = T_1/T_2$ and the ratio of the pumped areas $\kappa = A_1/A_2$ because these are the parameters of the system that can easily be modified in the experiment.

Note that unfortunately some parameters used in the numerical simulations have not been adapted precisely to the experimental setup presented in Sec. 3. This concerns predominantly the round-trip times and a small shift in the wavelengths affecting the employed effective cross sections. A quantitative comparison between the specific experiment in Sec. 3 and our simulation results is not intended. The aim of the model analysis is to explore the physical mechanism underlying the experimentally observed dynamics of the laser intensities in intra-cavity pumped thin-disk lasers in general. Therefore, the differences in the parameters are of no concern.

4. Results of the rate-equation model

4.1. Steady state solutions: continuous-wave lasing

We start our analysis by discussing the continuous-wave lasing states of the system. These are characterized by a constant output power and – in the language of nonlinear physics – thus correspond to steady state solutions of the dynamical system

$$\frac{\mathrm{d}}{\mathrm{d}\tau}\vec{x} = \vec{F}(\vec{x}) \qquad \text{with} \quad \vec{x} = \left[D_1, i_1, D_2, i_2\right]^T, \tag{13}$$

where the superscript ^{T} indicates the transpose of a vector and the function $\vec{F}$ is defined by the right hand sides of Eqs. (9)–(12). The stability of a steady state $\vec{x_0}$ fulfilling $\vec{F}(\vec{x_0}) = \vec{0}$ can in general be determined from a linear stability analysis [33]. The time evolution of a small deviation $\vec{\delta}$ from the steady state is investigated by expanding $\vec{F}$ around $\vec{x_0}$. The time evolution of $\vec{\delta}$ is then given by

$$\frac{\mathrm{d}}{\mathrm{d}\tau}\vec{\delta} = \left.\frac{\partial\vec{F}}{\partial\vec{x}}\right|_{\vec{x_0}}\vec{\delta}\,, \tag{14}$$

where $\left.\frac{\partial\vec{F}}{\partial\vec{x}}\right|_{\vec{x_0}}$ is the Jacobi matrix of the system containing the partial derivatives of the components of $\vec{F}$ evaluated at the steady state. The deviation from the state decreases with time and the steady state is thus stable, if the Jacobi matrix possesses only eigenvalues with negative real part. Otherwise, the steady state is unstable. Complex eigenvalues result in an oscillatory increase or damping of the deviation from the fixed point, e.g. damped relaxation oscillations in laser systems. In the following analysis, the steady state solutions are obtained by setting the right-hand side of Eqs. (9)–(12) to zero. In the derivation of the following Eqs. (15)–(19) from this condition, we neglect the spontaneous emission into the modes in very good approximation, i.e. use $\eta_1 \approx \eta_2 \approx 0$. Parameter continuation (see, e.g., [34] for a general reference to the method and, e.g., [35] for an application in the context of semiconductor lasers) is used to follow the solutions with varying control parameters and to simultaneously calculate the corresponding eigenvalues. To that end, we employ the continuation package MatCont [36,37], a toolbox for bifurcation analysis of dynamical systems.

We first determine the threshold diode pump intensity that is necessary to achieve continuous-wave emission of the second laser. Figure 6 shows the stable steady states of the system with varying diode pump intensity $i_{\mathrm{D},0}$. We find three qualitatively different regimes: For very low diode pump intensity (regime I), the lasing threshold of the first laser is not reached. In this case, the population density of disk 1 increases in good approximation linearly with the pumping. For higher diode pump intensities (regime II), the lasing threshold of the first laser is reached. Its

Optics EXPRESS

intensity i_1 and thus also the population density D_2 of disk 2 increases. When the diode pump intensity exceeds the threshold

$$i_{\mathrm{D},0,\mathrm{th}} = \frac{W_{\mathrm{D},1}}{B_1 M_{\mathrm{D},1}\{1-\exp[-W_{\mathrm{D},1}(1-D_1/B_1)]\}}\left[D_1 + \frac{M_{1,1}(D_1-1)D_2}{M_{1,2}\kappa(B_2-D_2)}\right], \tag{15}$$

both lasers are in continuous-wave operation (regime III) since the lasing threshold of the second laser is reached. In this regime, the population densities in the disks are clamped to the following values: In the second laser, the population density

$$D_2 = \frac{\gamma_{\mathrm{diss},2} + \gamma_{\mathrm{out},2}}{W_2} + 1 \tag{16}$$

is determined by an equilibrium between reabsorption in disk 2 on the one hand and (dissipative and outcoupling) losses on the other hand. Since disk 2 represents a loss for the first laser, the population density in disk 1

$$D_1 = 1 + \kappa\frac{M_{1,2}}{M_{1,1}}\left(1-\frac{D_2}{B_2}\right) - \frac{\gamma_{\mathrm{diss},1}}{W_1} \tag{17}$$

depends on the beam area ratio κ. The laser intensities in regime III are given by

$$i_1 = \frac{B_1 M_{\mathrm{D},1}}{M_{1,1}(D_1-1)W_{\mathrm{D},1}}\left\{1-\exp\left[-W_{\mathrm{D},1}\left(1-\frac{D_1}{B_1}\right)\right]\right\} i_{\mathrm{D},0} - \frac{D_1}{M_{1,1}(D_1-1)} \tag{18}$$

$$i_2 = \frac{M_{1,2}(B_2-D_2)\kappa}{M_{2,2}(D_2-1)} i_1 - \frac{D_2}{M_{2,2}(D_2-1)} \tag{19}$$

and both increase linearly with the diode pump intensity.

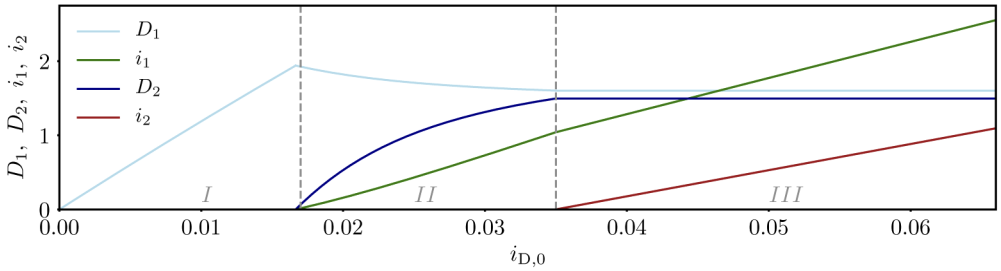

Fig. 6. Stable steady states as a function of the diode pump intensity. For low diode pump intensities, the lasing threshold of the first laser is not reached (regime I). With increasing diode pump intensity, the first laser reaches threshold and thus also the population density in disk 2 increases (regime II). When the lasing threshold of the second laser is reached for even higher diode pump intensity, the system is in continuous-wave lasing mode (regime III). The steady states in this figure are determined for $\chi = 1$ and $\kappa = 1$.

In the following, we fix the diode pumping intensity to $i_{\mathrm{D},0} = 0.0482$ corresponding to the pump power of 280 W used in the experiment and investigate the influence of the beam area ratio κ and the resonator round-trip time ratio χ on the continuous-wave emission. The corresponding steady states are shown in Fig. 7(a) and (b). Our experimental setup allows us to change the pumped area and beam area A_2 on disk 2 by changing the resonator length of the first laser. Let us assume we decrease the beam area A_2. This leads to higher intensity of the 1032 nm pump light that is incident onto the disk of the second laser, thus saturating its pump transition more strongly. If this disk were not sitting in an another resonator, it would be a conventional saturable

Optics EXPRESS

absorber and stronger saturation would lead to lower absorption of the 1032 nm laser light. Thus, the intra-cavity intensity i_1 would increase. However, the opposite is happening in our laser as can be seen from Fig. 7(a). The reason for this is that an increasing pump intensity on disk 2 pushes the second laser higher above its threshold. This leads to a higher intra-cavity intensity of this laser. The associated stronger stimulated emission re-populates the lower level of the laser atoms in disk 2 quickly, providing more atoms that can absorb the light from the first laser. The process can also be understood in terms of conservation of energy. Close inspection of Fig. 7(a) reveals that if κ is increasing by a factor of two from 1.0 to 2.0, the intensity i_2 is increasing by more than a factor of 2 (an increase from 0.49 to 1.08). The output power of the second laser is proportional to the product of the normalized intracavity intensity i_2 and the beam area A_2 in disk 2. Thus, the output power is increasing because i_2 is increasing by more than a factor of 2 and $A_2 = A_1/\kappa$ is decreasing by exactly a factor of 2. This additional power is taken from the dissipative losses of the intra-cavity power of the first laser which decrease if its intra-cavity power is decreasing.

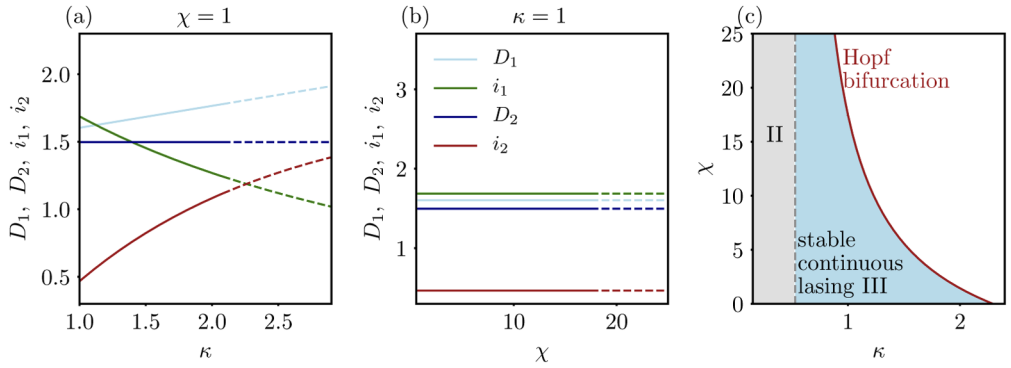

Fig. 7. Influence of the beam area ratio κ and the resonator round-trip time ratio χ on the steady state corresponding to continuous-wave emission. Solid (dashed) lines indicate stable (unstable) states. (a) When κ is increased at fixed $\chi = 1$, the steady state changes and looses stability in a Hopf bifurcation at $\kappa \approx 2.08$. (b) When χ is increased at fixed $\kappa = 1$, the stationary state looses stability in a Hopf bifurcation at $\chi = 17.461$. (c) The parameter region for which the continuous-wave emission is stable (blue region, III) is confined by the Hopf bifurcation line (red line) to the right. To the left, the lasing threshold of the second laser is not reached (grey region, II).

When κ is increased beyond a given threshold κ_H – in the language of nonlinear physics called a bifurcation point – the steady state corresponding to the continuous-wave emission looses stability. For $\kappa<\kappa_H$, all four eigenvalues of the system have negative real parts and the fixed point is stable (solid lines). At the bifurcation point $\kappa_H \approx 2.081$, two eigenvalues $\lambda_\pm = \pm 155.6i$ simultaneously cross the imaginary axis. This eigenvalue structure is characteristic for a Hopf bifurcation. For $\kappa>\kappa_H$, deviations from the steady state oscillatory increase due to the positive real parts of the two eigenvalues and the state is unstable (dashed lines). A small-amplitude periodic self-sustained oscillation with period $T = 2\pi/Im(\lambda_+)$ replaces the fixed point as stable attractor as we will discuss in more detail in the next section.

Figure 7(b) shows that the ratio of the resonator round-trip times χ does not influence the population densities and intensities, as expected from Eqs. (16)–(19). However, it affects the stability of the state. For $\kappa = 1$, the steady state becomes unstable in a Hopf bifurcation which occurs at $\chi_H = 17.461$ with eigenvalues $\lambda_\pm = \pm 174.8i$.

Figure 7(c) summarizes the influence of κ and χ on the stability of the continuous-wave emission. For small values of κ (grey region, II), the lasing threshold of the second laser is

Optics EXPRESS

not reached. The limiting grey dashed line is determined by Eq. (15). For larger values of κ, the continuous-wave emission is stable (blue region, III). The Hopf bifurcation line (red), i.e. the parameter tuple (κ_H, χ_H) for which the two eigenvalues cross the imaginary axis, limits the parameter region for stable continuous-wave emission to the other side. Beyond the red bifurcation line (white region), the intensity starts to show periodic self-sustained oscillations, pulse trains and chaotic emission which we discuss now in more detail.

4.2. Periodic solutions: self-sustained oscillations and pulse trains

To study the dynamics of the system in the oscillatory regime, Eqs. (9)–(12) are integrated numerically with an explicit Runge-Kutta method of order 5(4). These time simulations are performed for a time span of $\Delta\tau_t = 150$ to remove transient behavior. Then, the local maxima of the population densities and intensities are analyzed for a subsequent time span $\Delta\tau = 20$. We investigate the effect of the beam area ratio on the dynamics by performing time simulation for so-called *adiabatically* increasing values of κ, i.e. the end state of a simulation run is taken as initial condition for the next simulation with slightly higher value of κ. The model qualitatively reproduces the self-sustained oscillations and pulse trains that are observed experimentally for comparable beam area ratios κ (cf. Fig. 3). The details of the bifurcation scenario, like the exact value of κ, differ between the model and the experiment. This is to be expected due to the approximations in the model and the large number of parameters that enter the rate-equations.

Figure 8(a) shows the local maxima of the intensities i_1 and i_2. Exemplary solutions for three parameter values of κ are shown in Fig. 8(b) - (d), respectively. As expected, the system is in the steady state corresponding to stable continuous-wave emission for small values of κ. Note that i_1 and i_2 in Fig. 8(a) are for κ<2.081 small but not zero. Figure 7(a) shows these intensities on a larger scale. Continuous-wave emission looses stability in a Hopf bifurcation at $\kappa = \kappa_{\mathrm{H}} \approx 2.081$ as discussed above. A small-amplitude periodic oscillation around the fixed point arises that is shown in Fig. 8(b). The period of the oscillation is $T = 0.0404$, fitting to the eigenvalues $\lambda_{\pm} = \pm 155.6i$ at the bifurcation point. The region of stability of this small-amplitude oscillation is, however, rather small and for slightly larger values of κ, it is replaced by pulse trains with pronounced intensity peaks. For $2.09 \leq \kappa \leq 2.27$, the dynamics of the system is a 3P-1P cycle which exhibits three intensity pulses in i_1 with different local maxima followed by one pulse in i_2 (see Fig. 8(c)). With increasing value of κ, the system goes through a 2P-2P cycle in a small parameter region and a 2P-1P cycle (see Fig. 8(d)). For large values of $\kappa \geq 2.8$, the system is in a 1P-1P cycle with high peak intensity. In an experiment, these solutions with high peak intensities could potentially be useful for materials processing but could also damage the dielectric coatings on the disks.

The dynamics of the intensities and population densities for the 2P-1P cycle shown in Fig. 8(d) allows us to understand the emergence of the high peak intensities. At the beginning of the cycle, the intensities of both lasers are low. Disk 1 is pumped continuously and the population of the excited state rises. The excited state in disk 2 is still occupied from the previous cycle but the population density decreases due to spontaneous emission. After some time, disk 1 reaches the lasing threshold. The intensity in disk 1 thus increases rapidly within a few microseconds. The intensity of the first laser bleaches disk 2, thereby further accelerating its increase of intensity. At the same time, the amplification of disk 1 decreases because the intensity reaches values up to 60 times larger than its saturation intensity and finally this laser falls below the lasing threshold. This sequence repeats multiple times in one cycle and with each repetition, the population of the excited state of disk 2 increases stepwise. When the amplification of disk 2 overcomes the losses, the intensity in disk 2 rapidly increases, also reaching multiples of the saturation value. The intensity saturates the amplification of disk 2 and in consequence, it falls below the lasing threshold. Then, the cycle repeats itself. The repetition rate of the pulse trains is constant for a given parameter set and is determined by the period of the respective limit cycle. Varying a

Optics EXPRESS

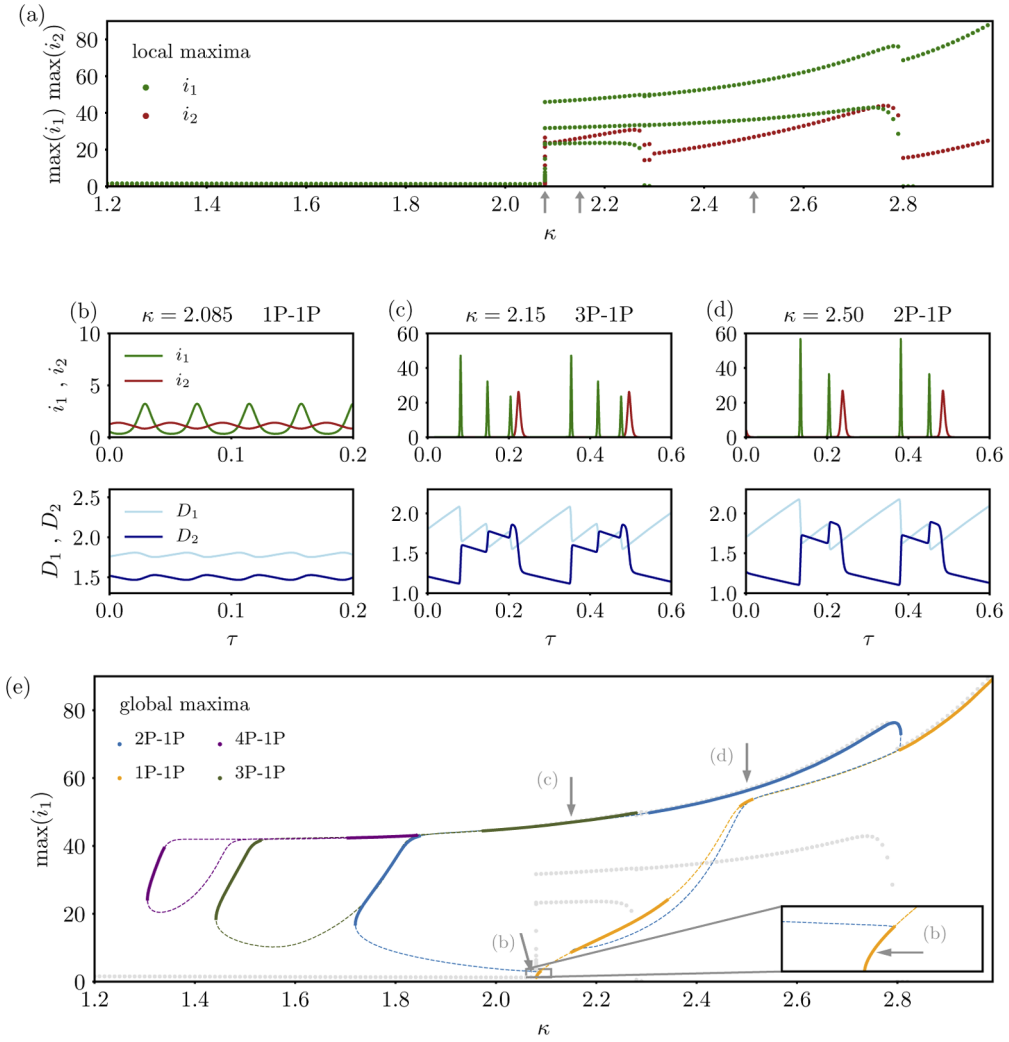

Fig. 8. Periodic solutions of the system corresponding to self-sustained oscillations and pulse trains. (a) Local maxima of the intensities i_1 (green) and i_2 (red) obtained by time simulations. The value of κ is increased "adiabatically", i.e. the end state of a simulation run is taken as initial condition for the next one. For κ<2.081, the laser is in stable continuous-wave mode and the intensities are temporally constant. For larger values of κ, periodic solutions with intensity peaks occur. Exemplary periodic cycles for three parameter values of κ marked by grey arrows in (a) are presented in (b)-(d). The global maxima of i_1 obtained by parameter continuation of solutions with one intensity peak in i_2 and up to four peaks in i_1 are shown in (e). Solid (dashed) lines indicate stable (unstable) states. The local maxima of the stable solutions for i_1 obtained in the time simulations (cf. (a)) are shown with grey dots for comparison. The arrows indicate the location of the solutions (b) - (d) on the periodic solution branches. The resonator round-trip time ratio is set to $\chi = 1$.

Optics EXPRESS

single parameter of the system in general affects not only the repetition rate but also other aspects of the dynamics, like the peak intensities.

Due to the potentially useful as well as damaging nature of the periodic cycles with high peak intensities, it is important to understand their region of existence and stability. To this end, we employ parameter continuation. Starting from a solution of the system found by time simulation for a given parameter value (here of the beam size ratio κ), the technique allows us to follow the solution when the parameter is varied. It is not necessary to perform time simulations starting from various initial conditions for each parameter value [34]. For example, we can start with the 3P-1P solution for $\kappa = 2.15$ which we have found by time simulation (cf. Fig. 8(a) and (c)). We then continue to reduce the parameter κ. This leads to new solutions not found in the time simulations in Fig. 8(a) as we will now show. In this way, we can systematically investigate for which parameter region a solution type (e.g. 3P-1P cycle) exists. In addition to stable solutions, parameter continuation also reveals unstable solutions that are not observable experimentally and in time simulations. The stability of an obtained periodic cycle can be determined from the respective Floquet multipliers [38]. However, parameter continuation does not predict the so-called basin of attraction of stable solutions, i.e. for which initial conditions the system actually evolves into the stable solution.

Our analysis via parameter continuation shows that the solution space of the system is very rich, i.e. the laser system can exhibit a multitude of periodic cycles even for the same value of κ. Here, we restrict ourselves to periodic cycles with one intensity peak in i_2 and up to four peaks in i_1. Figure 8(e) shows the global maxima of the intensity i_1 for the periodic cycles obtained by parameter continuation. Stable solutions are shown with solid lines, unstable solutions which are not expected to be observed in an experiment for an extended time-span are shown with dashed lines. The local intensity maxima of i_1 obtained in the time simulations presented in Fig. 8(a) are shown again in Fig. 8(e) with grey dots for comparison. If a periodic cycle obtained by parameter continuation is also observed in the time simulations for the respective value of κ, the global maximum of i_1 (solid line) coincides with the largest local maximum (grey dots). This is e.g. the case for the solutions (c) and (d) marked by arrows.

The parameter continuation confirms the emergence of a stable small-amplitude 1P-1P cycle (orange) from the steady state at $\kappa \approx 2.081$ which rapidly looses stability when κ is further increased. It also verifies the existence of 2P-1P (blue) and 3P-1P (green) cycles corresponding to pulse trains with large intensity maxima. The stability analysis shows that the 2P-1P and 3P-1P cycles are also stable in extended parameter regions for κ<2.081. In addition, a stable 4P-1P cycle (purple) is found in this parameter range. Note that for κ<2.081, periodic dynamics and in particular the 4P-1P cycle are not observed in the time simulations with adiabatically increased κ (cf. Fig. 8(a)). Instead, the system is in the steady state corresponding to continuous-wave emission for this parameter regime. The system thus shows multi-stability, i.e. multiple solutions are stable for the same parameter set. For example, Fig. 8(e) shows that for $\kappa = 1.75$ a stable 4P-1P cycle as well as a stable 2P-1P cycle exists. Figure 8(a) shows that continuous-wave emission is also stable for this beam area ratio. The observed dynamics of the lasers, i.e. whether they are in stable continuous-wave operation or show pulse trains, depends on the initial condition and thus on their history. We observe a hysteresis of the transition from stable continuous-wave operation to oscillatory emission when the beam area ratio κ is first adiabatically increased from $\kappa = 1.9$ to $\kappa = 2.2$ (cf. Fig. 8(a), transition from stable continuous-wave emission to oscillations at $\kappa_H \approx 2.081$) and subsequently adiabatically decreased again (data not shown). For decreasing κ, the dynamics of the system remains oscillatory in the range $1.95 \leq \kappa \leq 2.081$, before falling back to stable continuous-wave emission.

Optics EXPRESS

4.3. Chaotic states

In this section, we analyze the system for an initial condition that reveals the full richness of its dynamics. Figure 9 shows the local maxima of the laser intensities, now starting the time simulation run from the initial condition $(i_1, D_1, i_2, D_2) = (0, 0, 0, 0)$ for each value of the beam area ratio κ. For ratios of the pumped areas κ larger than 2.081, the dynamical behavior of the system is qualitatively identical to the one observed for "adiabatically" increased κ (cf. Fig. 8(a)). For smaller beam area ratios in the range $1.67 \leq \kappa \leq 2.081$, the dynamics of the system is, however, rather different. The system does not evolve into the stable continuous-wave lasing state for the initial condition $(i_1, D_1, i_2, D_2) = (0, 0, 0, 0)$ in this parameter range. Instead, we observe the 4P-1P periodic solution for $1.68 \leq \kappa \leq 1.82$ that was found to be stable in this parameter range by parameter continuation (cf. purple line in Fig. 8(e)). This observation again demonstrates the multi-stability of the system and the dependence of the observed dynamics on the initial condition.

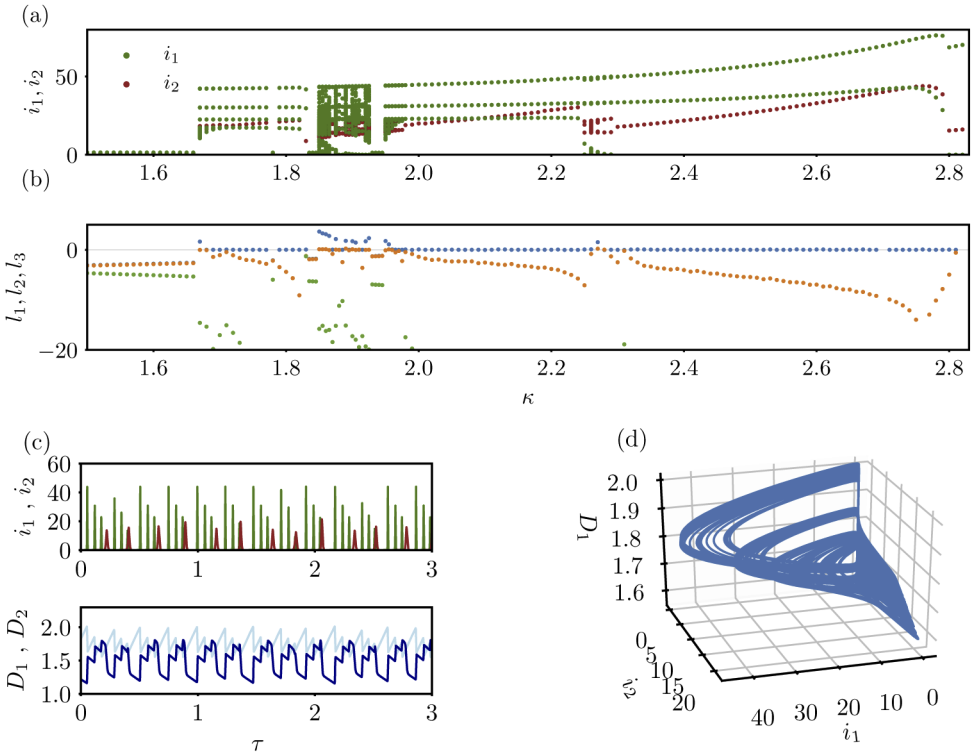

Fig. 9. Chaotic intensity fluctuations. (a) Local maxima of the intensities $i_1(t)$ (green) and $i_2(t)$ (red) obtained by time simulations. In contrast to the results shown in Fig. 8(a), each simulation run was started from the initial condition $(i_1, D_1, i_2, D_2) = (0, 0, 0, 0)$. (b) The signs of the three largest Lyapunov exponents (l_1, l_2, l_3) can be used to identify the type of dynamics. Positive Lyapunov exponents indicate chaotic dynamics. (c) Exemplary chaotic solution for $\kappa = 1.92$ and (d) corresponding attractor projected to the (i_1, i_2, D_1) phase space.

For some beam area ratios in the range of $1.85 \leq \kappa \leq 1.95$, the laser intensities do not have a small number of distinct local maxima. An exemplary solution for $\kappa = 1.92$ together with a projection of the respective attractor in the (i_1, i_2, D_1) phase space is shown in Fig. 9(c) and (d). The dynamics consists of intensity peaks in i_1 followed by a peak in i_2 where the magnitudes of the peaks vary unpredictably from cycle to cycle. The output power of the laser system fluctuates

Optics EXPRESS

chaotically. This type of dynamics was also observed experimentally for certain large beam area ratios κ (cf. Fig. 3 and Fig. 4).

To substantiate the observation that the system exhibits regions of chaotic dynamics for certain beam area ratios, we determine the Lyapunov exponents [38]. They qualitatively measure the time-averaged exponential rate of divergence or convergence of volume elements in phase space and are a well-established tool for dynamic systems. Depending on the signs of the largest two exponents, different qualitative types of dynamics can be distinguished: If the system evolves towards a stationary fixed point, the difference between initially slightly different states decreases over time and the two largest Lyapunov exponents are negative. For periodic dynamics, the largest Lyapunov exponent is zero. If the dynamics is chaotic and therefore highly sensitive to the initial condition, at least one Lyapunov exponent is positive. Figure 9(b) shows the largest three Lyapunov exponents (l_1, l_2, l_3) of the system calculated numerically via the Wolf algorithm [39]. The determined Lyapunov exponents confirm that depending on the beam area ratio κ, the system exhibits regions of stable continuous-wave lasing ($l_1<0$ and $l_2<0$), periodic pulse trains ($l_1 = 0$ and $l_2<0$) and chaotic intensity fluctuations ($l_1>0$ and $l_2 = 0$) which were also observed experimentally (cf. Fig. 3(e) and Fig. 4). Due to the large number of parameters in the rate equations, the model can not be expected to capture the onset of chaotic intensity fluctuations quantitatively, but it predicts chaos for beam area ratios in the same order of magnitude as in the experiment. This shows that chaotic emission is an inherent feature of this laser system that does not arise due to external perturbations and noise.

In sections 4.2 and 4.3, we have varied the beam area ratio κ and kept all other parameters of the model fixed. We would like to point out that the destabilization of continuous-wave emission can also be achieved by increasing the normalized diode pump intensity $i_{D,0}$ (data not shown) which can lead to pulse trains and chaotic dynamics. This was also observed in the experiment where stronger diode pumping resulted in intensity peaks that potentially damage the laser disks.

5. Conclusion

We showed that an intra-cavity pumped Yb:YAG thin-disk laser is capable of various types of dynamics that can be controlled by a single experimental parameter, namely the resonator length of the diode-pumped laser. This parameter affects the ratio of the beam areas on the disks and, to a lesser extent, the ratio of the resonator round-trip times. Experimentally, continuous-wave emission, periodic pulse trains and chaotic power fluctuations were observed. We presented a rate-equation model capable of qualitatively reproducing all these types of dynamics and investigated it in the framework of nonlinear dynamics. The investigation of this deterministic model confirms that the dynamics of the laser system arises due to intrinsic properties of the system and is not driven by external perturbations. Periodic pulses and chaotic fluctuations are a result of the strong coupling between the first, diode-pumped laser and the second, intra-cavity pumped laser which acts as a saturable absorber. We found that the beam area ratio affects this coupling because it determines the saturation and thus also determines the output dynamics. The observation that continuous-wave emission becomes unstable for large beam area ratios substantiates the idea that focusing on maximal optical efficiency is not sufficient for the design of intra-cavity pumped laser systems: Stability is another criterion for the optimal set-up. The observed multi-stability in the intra-cavity pumped Yb:YAG thin-disk laser shows that whether a laser system exhibits stable continuous-wave emission does not only depend on the parameters of the system, but also on its initial condition.

Funding. Deutsche Forschungsgemeinschaft (WI 1939/4-1).

Acknowledgements. We gratefully acknowledge the support of Trumpf GmbH & Co. KG.

Disclosures. The authors declare no conflicts of interest.

References

Optics EXPRESS

1. F. Arecchi, G. Lippi, G. Puccioni, and J. Tredicce, "Deterministic chaos in laser with injected signal," Opt. Commun. **51**(5), 308–314 (1984).
2. T. Erneux and P. Glorieux, *Laser dynamics* (Cambridge University, 2010).
3. C. Bollig, R. Hayward, W. Clarkson, and D. Hanna, "2-W Ho:YAG laser intracavity pumped by a diode-pumped Tm:YAG laser," Opt. Lett. **23**(22), 1757–1759 (1998).
4. M. Schellhorn, A. Hirth, and C. Kieleck, "Ho:YAG laser intracavity pumped by a diode-pumped Tm:YLF laser," Opt. Lett. **28**(20), 1933–1935 (2003).
5. X. Yang, H. Huang, D. Shen, H. Zhu, and D. Tang, "2.1 μm Ho:LuAG ceramic laser intracavity pumped by a diode-pumped Tm:YAG laser," Chin. Opt. Lett. **12**(12), 121405–121408 (2014).
6. Y. Chen, H. Wang, J. Dong, M. Wang, H. Chen, Y. Qian, G. Zhu, K. Alekse, and X. Zhu, "Tm:YAG disk laser intra-cavity pumped by QCW 1μm Yb:YAG thin disk laser," IEEE Photonics Technol. Lett. **31**(14), 1139–1142 (2019).
7. C. Vorholt and U. Wittrock, "Intra-cavity pumped Yb:YAG thin-disk laser with 1.74% quantum defect," Opt. Lett. **40**(20), 4819–4822 (2015).
8. A. Brenier, Y. Guyot, H. Canibano, G. Boulon, A. Ródenas, D. Jaque, A. Eganyan, and A. G. Petrosyan, "Growth, spectroscopic, and laser properties of Yb^3 +-doped $Lu_3Al_5O_12$ garnet crystal," J. Opt. Soc. Am. B **23**(4), 676–683 (2006).
9. J. Koerner, C. Vorholt, H. Liebetrau, M. Kahle, D. Kloepfel, R. Seifert, J. Hein, and M. C. Kaluza, "Measurement of temperature-dependent absorption and emission spectra of Yb:YAG, Yb:LuAG, and Yb:CaF_2 between 20°C and 200°C and predictions on their influence on laser performance," J. Opt. Soc. Am. B **29**(9), 2493–2502 (2012).
10. C. Vorholt and U. Wittrock, "Self-sustained pulsations in an intra-cavity pumped thin-disk laser," in *2015 European Conference on Lasers and Electro-Optics - European Quantum Electronics Conference*, (Optical Society of America, 2015), p. CA_P_10.
11. R. Kohn, C. Shank, E. Ippen, and A. Dienes, "An intracavity-pumped CW dye laser," Opt. Commun. **3**(3), 177–178 (1971).
12. V. Gapontsev, M. Zhabotinskii, A. Izyneev, V. Kravchenko, and Y. P. Rudnitskii, "Effective 1.054? 1.54 μ stimulated emission conversion," JETP Lett. **18**, 251 (1973).
13. R. Stoneman and L. Esterowitz, "Intracavity-pumped 2.09-μm Ho: YAG laser," Opt. Lett. **17**(10), 736–738 (1992).
14. K. Spariosu and M. Birnbaum, "Intracavity 1.549-μm pumped 1.634-μm Er:YAG lasers at 300 K," IEEE J. Quantum Electron. **30**(4), 1044–1049 (1994).
15. R. Hayward, W. Clarkson, and D. Hanna, "High-power diode-pumped room-temperature Tm:YAG and intracavity-pumped Ho:YAG lasers," in *Advanced Solid State Lasers*, (Optical Society of America, 2000), p. MB8.
16. M. Schellhorn and A. Hirth, "Modeling of intracavity-pumped quasi-three-level lasers," IEEE J. Quantum Electron. **38**(11), 1455–1464 (2002).
17. S. So, J. Mackenzie, D. Shepherd, W. Clarkson, J. Betterton, E. Gorton, and J. Terry, "Intra-cavity side-pumped Ho:YAG laser," Opt. Express **14**(22), 10481–10487 (2006).
18. E. Herault, F. Balembois, P. Georges, and T. Georges, "1064 nm Nd:YVO_4 laser intracavity pumped at 912 nm and sum-frequency mixing for an emission at 491 nm," Opt. Lett. **33**(14), 1632–1634 (2008).
19. Y. Lü, J. Xia, X. Yin, D. Wang, and X. Zhang, "1085 nm Nd:YVO_4 laser intracavity pumped at 914 nm and sum-frequency mixing to reach cyan laser at 496 nm," Laser Phys. Lett. **7**(1), 11–13 (2010).
20. Y. Lü, J. Xia, and X. Zhang, "1064 nm Nd:YAG laser intracavity pumped at 946 nm," Laser Phys. **20**(4), 766–768 (2010).
21. Y. Lü, X. Zhang, J. Xia, R. Chen, G. Jin, J. Wang, C. Li, and Z. Ma, "981 nm Yb:KYW laser intracavity pumped at 912 nm and frequency-doubling for an emission at 490.5 nm," Laser Phys. Lett. **7**(5), 343–346 (2010).
22. G. Zhu, X. He, B. Yao, and Y. Wang, "Ho:YAP laser intra-cavity pumped by a diode-pumped Tm:YLF laser," Laser Phys. **23**(1), 015002 (2013).
23. E. J. Saarinen, E. Vasileva, O. Antipov, J.-P. Penttinen, M. Tavast, T. Leinonen, and O. G. Okhotnikov, "2-μm Tm:Lu_2O_3 ceramic disk laser intracavity-pumped by a semiconductor disk laser," Opt. Express **21**(20), 23844–23850 (2013).
24. Z. Yang, J. Meng, A. R. Albrecht, and M. Sheik-Bahae, "Radiation-balanced Yb:YAG disk laser," Opt. Express **27**(2), 1392–1400 (2019).
25. C. Vorholt and U. Wittrock, "Wavelength control by angle-tuning of the laser radiation in an intra-cavity pumped Yb:YAG thin-disk laser," in *Advanced Solid State Lasers*, (Optical Society of America, 2015), p. AM5A.39.
26. C. Vorholt and U. Wittrock, "Spatial hole burning in Yb:YAG thin-disk lasers," Appl. Phys. B **120**(4), 711–721 (2015).
27. J. Perchermeier and U. Wittrock, "Precise measurements of the thermo-optical aberrations of an Yb:YAG thin-disk laser," Opt. Lett. **38**(14), 2422–2424 (2013).
28. D. Brown, "Rigrod laser-pumped-laser resonator model: I. Theoretical considerations," Laser Phys. **24**(8), 085002 (2014).
29. D. Brown, "Rigrod laser-pumped-laser resonator model: II. Application to thin and optically-dilute laser media," Laser Phys. **24**(8), 085003 (2014).
30. K. Contag, "Modellierung und numerische Auslegung des Yb:YAG-Schreibenlasers," Ph.D. thesis, Universität Stuttgart (2002).

Optics EXPRESS

31. D. S. Sumida and T. Y. Fan, "Emission spectra and fluorescence lifetime measurements of Yb:YAG as a function of temperature," in *Advanced Solid State Lasers*, (Optical Society of America, 1994), p. YL4.
32. R. Paschotta, "RP Photonics, Encyclopedia of laser physics and technology," Available on: https://www.rp-photonics.com/saturation-power.html (2020).
33. S. H. Strogatz, *Nonlinear dynamics and chaos: with applications to physics, biology, chemistry, and engineering* (Westview, 2001).
34. Y. A. Kuznetsov, *Elements of applied bifurcation theory*, vol. 112 (Springer Science & Business Media, 2013).
35. S. Wieczorek, B. Krauskopf, T. B. Simpson, and D. Lenstra, "The dynamical complexity of optically injected semiconductor lasers," Phys. Rep. **416**(1-2), 1–128 (2005).
36. W. Govaerts, Y. A. Kuznetsov, and A. Dhooge, "Numerical continuation of bifurcations of limit cycles in MATLAB," SIAM J. Sci. Comput. **27**(1), 231–252 (2005).
37. A. Dhooge, W. Govaerts, and Y. A. Kuznetsov, "MATCONT: a MATLAB package for numerical bifurcation analysis of odes," ACM Trans. Math. Softw. **29**(2), 141–164 (2003).
38. J. H. Argyris, G. Faust, M. Haase, and R. Friedrich, *An Exploration of Dynamical Systems and Chaos: Completely Revised and Enlarged Second Edition* (Springer, 2015).
39. A. Wolf, J. B. Swift, H. L. Swinney, and J. A. Vastano, "Determining Lyapunov exponents from a time series," Phys. D **16**(3), 285–317 (1985).